https://doi.org/10.3311/PPee.37384

Periodica Polytechnica Electrical Engineering and Computer Science

An Improved BS_NAHOSM Hybrid Control Strategy for FOC of Dual Star Induction Motor Drives

Ngoc Thuy Pham[1*]

[1] Laboratory of Electric Drives, Faculty of Electrical Engineering Technology, Industrial University of Ho Chi Minh City, 12 Nguyen Van Bao street, Go Vap District, 700000 Ho Chi Minh, Vietnam
[*] Corresponding author, e-mail: phamthuyngoc@iuh.edu.vn

Received: 16 May 2024, Accepted: 26 May 2025, Published online: 01 July 2025

Abstract

In this paper, a novel adaptive hybrid control structure for field-oriented control (FOC) of six-phase induction motor (SPIM) drives is proposed. The controller effectively integrates backstepping (BS) control for the outer loops with a novel adaptive higher-order sliding mode (NAHOSM) controller for the inner current loop. This control strategy also proposes load disturbance estimator using a predictive model to estimate the component required for the BS_NAHOSM control strategy to help identify and proactively eliminate disturbances. The proposed approach demonstrates robust and stable performance under parameter uncertainties and load disturbances, while significantly reducing the chattering phenomenon. Simulation results obtained using MATLAB/Simulink confirm the effectiveness and superiority of the proposed control strategy.

Keywords

backstepping control, sliding mode control, high orsder sliding mode control, six-phase induction motor drives, FOC control

1 Introduction

The six-phase induction motor (SPIM) has emerged as a prominent solution among multiphase Alternating Current (AC) drive systems due to its enhanced reliability, fault tolerance, and operational stability. Over recent decades, SPIM technology has garnered significant research interest and has been widely adopted in high-capacity industrial applications requiring robust and dependable performance [1]. Owing to these advantages, SPIM is increasingly replacing traditional three-phase induction motors (IM), even in small power applications where high precision, safety, and reliability are crucial.

In recent years, control strategies for AC and SPIM drives have evolved toward advanced vector control techniques, among which field-oriented control (FOC) remains one of the most widely implemented methods [2]. Despite its benefits, FOC performance is highly sensitive to variations in motor parameters and external load disturbances. Conventional Proportional Integral Derivative (PID) controllers with fixed parameters are often inadequate for high-performance drive systems [3]. To overcome these limitations, various nonlinear and intelligent control methods have been introduced [4–16], including sliding mode (SM) control, backstepping (BS), fuzzy logic, neural networks, model predictive control, and other control methods.

However, relying solely on a single control method has proven insufficient in ensuring optimal performance, especially for nonlinear systems. This challenge has led to growing interest in hybrid control strategies that combine the strengths of multiple control approaches [17–23]. For example, the hybrid BS–SM control structure proposed in Pham [20] effectively aligns with the design requirements of FOC-based SPIM systems. In this structure, SM is employed for the inner current loop due to its robustness, fast dynamic response, and precise reference tracking. Nevertheless, a major drawback of SM is the chattering phenomenon, which can degrade system performance and damage actuators.

Various techniques have been developed to mitigate chattering, such as introducing exponential or sigmoid functions, but these often compromise system stability and slow down convergence. The integral sliding mode (INTSM) method improves steady-state accuracy and disturbance rejection but may suffer from integral

Cite this article as: Pham, N. T. "An Improved BS_NAHOSM Hybrid Control Strategy for FOC of Dual Star Induction Motor Drives", Periodica Polytechnica Electrical Engineering and Computer Science, 2025. https://doi.org/10.3311/PPee.37384

saturation and large overshoots, with limited impact on chattering reduction. Other advanced approaches, including higher-order sliding mode (HOSM), second-order sliding mode (SOSM), and the super-twisting algorithm (STA), have also been proposed. Comparative studies show that STA offers faster convergence and improved tracking performance compared to SOSM, albeit at the cost of increased chattering, while SOSM provides better robustness with reduced chattering levels [24].

Building on this foundation, the present study proposes an enhancement of the BS–SM hybrid structure in Pham [20] by incorporating the STA into an improved high-order sliding mode framework (NAHOSM) for the inner current loop. The main objective of the NAHOSM strategy is the incorporation of an adaptive gain mechanism within the HOSM controller, reflecting its self-tuning capability. This mechanism employs a real-time gain adaptation law that allows the controller to autonomously determine the appropriate control gain based on current system conditions, without requiring prior knowledge of the bounds of uncertainties or disturbances. Such adaptability greatly simplifies the design process and enhances the controller's practical applicability. By continuously adjusting the gain to match varying operating conditions and IM parameter fluctuations, the control effort is optimized, resulting in a substantial reduction in both the amplitude and switching frequency of the control signals. This, in turn, significantly mitigates the chattering effect – a common drawback in conventional sliding mode controllers – while maintaining system stability and ensuring fast convergence. Overall, the adaptive NAHOSM strategy enables the control system to respond more effectively to dynamic uncertainties and disturbances, leading to more precise speed regulation and improved robustness under real-world operating conditions.

New points in this study:

- The development of a novel adaptive hybrid current control strategy, termed novel adaptive higher-order sliding mode (NAHOSM), which enhances the performance of high-order sliding mode control in the inner current loop for FOC of SPIM drive systems.
- The integration of a predictive torque estimation mechanism into the BS_NAHOSM control structure. This mechanism utilizes a forward Euler discretization-based predictive model to estimate the electromagnetic torque quickly and accurately. As a result, it enables the controller to proactively identify and reject disturbances, while effectively minimizing oscillations in the estimated torque signal.

The remainder of the paper is presented as follows. Section 2 presents the mathematical model of the SPIM drives, the proposed controller design is presented in detail in Section 3. Simulation results are presented in Section 4. Section 5 concludes the results.

2 The vector control model of SPIM drives

This drive system consists of a SPIM supplied by a six-phase voltage source inverter (SPVSI). The diagram of SPIM powered by SPVSI is shown in Fig. 1. In Section 2, the vector space decomposition (VSD) technique has also been applied as in Finch and Giaouris [2], the original six-dimensional space of SPIM is converted into three two-dimensional spaces in the stationary frame of reference (D–Q), (x–y) and (z_1–z_2). This transformation is obtained using a 6 × 6 transformation matrix [1]:

$$\boldsymbol{T}_6 = \frac{1}{3}\begin{bmatrix} 1 & \frac{\sqrt{3}}{2} & -\frac{1}{2} & -\frac{\sqrt{3}}{2} & -\frac{1}{2} & 0 \\ 0 & \frac{1}{2} & \frac{\sqrt{3}}{2} & \frac{1}{2} & -\frac{\sqrt{3}}{2} & -1 \\ 1 & -\frac{\sqrt{3}}{2} & -\frac{1}{2} & \frac{\sqrt{3}}{2} & -\frac{1}{2} & 0 \\ 0 & \frac{1}{2} & -\frac{\sqrt{3}}{2} & \frac{1}{2} & \frac{\sqrt{3}}{2} & -1 \\ 1 & 0 & 1 & 0 & 1 & 0 \\ 0 & 1 & 0 & 1 & 0 & 1 \end{bmatrix}. \quad (1)$$

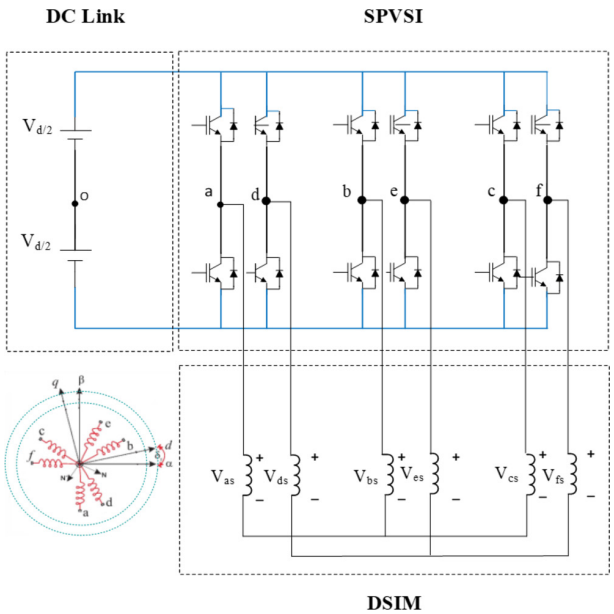

Fig. 1 A general scheme of an SPIM drive

SPIM's mathematical equations are written in a stationary reference frame as follows (Eq. (2)):

$$\begin{aligned}[V_s]&=[R_s][I_s]+P([L_s][I_s]+[L_m][I_r])\\ 0&=[R_r][I_r]+P([L_r][I_r]+[L_m][I_s])\end{aligned}, \tag{2}$$

where: $[V]$, $[I]$, $[R]$, $[L]$ and $[L_m]$ are voltage, current, resistant, self and mutual inductance matrices, respectively. P is differential operator, r and s related to the resistance of rotor and stator, respectively. Since the rotor is squirrel cage, $[V_r]$ is equal to zero.

The electromechanical conversion only takes in the (D–Q) subspace, (x–y) and (z_l–z_2) subspace just produce losses. Therefore, the control is based on determining the applied voltage in the D–Q reference frame. So SPIM control now is similar to the classical ACIM FOC. The voltage space vectors and switching states in the (D–Q) and (x–y) subspaces for a SPVSI are shown in Fig. 2. The control for the motor in the stationary reference frame is difficult, even for a three phase IM, so the transformation of SPIM model in a dq rotating reference frame to obtain currents with direct current (DC) components is necessary, a transformation matrix must be used to represent the stationary reference fame (D–Q) in the dynamic reference (D–Q). This matrix is given:

$$\boldsymbol{T}_{dq}=\begin{bmatrix}\cos(\delta_r) & -\sin(\delta_r)\\ \sin(\delta_r) & \cos(\delta_r)\end{bmatrix}, \tag{3}$$

where δ_r is the rotor angular position referred to the stator that shows in Fig. 1.

The FOC is the most used strategy in the industrial field. In this control method, the rotor flux is controlled by $\boldsymbol{i}_{sd}$ stator current component and the torque by $\boldsymbol{i}_{sq}$ quadratic component. We have: $\boldsymbol{\psi}_{rq}=0$; $\boldsymbol{\psi}_{rd}=\boldsymbol{\psi}_{rd}$. The model motor

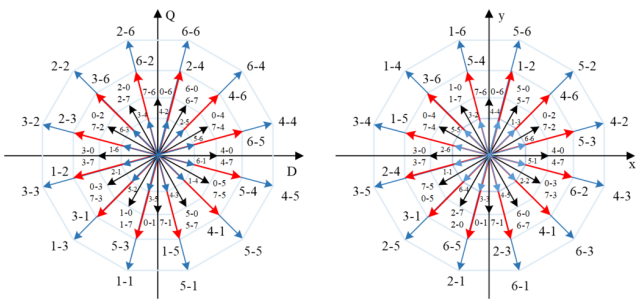

Fig. 2 Voltage space vectors and switching states in the (D–Q) and (x–y) subspaces for a SPVSI

dynamics is described by the following space vector differential equations:

$$\begin{cases}\dfrac{d\omega}{dt}=\dfrac{3}{2}n_p\dfrac{\delta\sigma\boldsymbol{L}_s}{J}\left(\boldsymbol{\psi}_{rd}\boldsymbol{i}_{sq}\right)-\dfrac{T_L}{J}-B\omega\\ \dfrac{d\boldsymbol{\psi}_{rd}}{dt}=\dfrac{\boldsymbol{L}_m}{\tau_r}\boldsymbol{i}_{sd}-\dfrac{1}{\tau_r}\boldsymbol{\psi}_{rd}\\ \boldsymbol{L}_s\dfrac{d\boldsymbol{i}_{sd}}{dt}=a\boldsymbol{i}_{sd}+\boldsymbol{L}_s\omega_s\boldsymbol{i}_{sq}+b\boldsymbol{R}_r\boldsymbol{\psi}_{rd}+c\boldsymbol{u}_{sd}\\ \boldsymbol{L}_s\dfrac{d\boldsymbol{i}_{sq}}{dt}=-a\boldsymbol{i}_{sq}+\boldsymbol{L}_s\omega_s\boldsymbol{i}_{sd}+b_r\omega_r\boldsymbol{\psi}_{rd}+c\boldsymbol{u}_{sq}\end{cases}, \tag{4}$$

where:

$$\sigma=1-\frac{\boldsymbol{L}_m^2}{\boldsymbol{L}_s\boldsymbol{L}_e};\ a=\frac{\boldsymbol{L}_m^2\boldsymbol{R}_r+\boldsymbol{L}_r^2\boldsymbol{R}_s}{\sigma\boldsymbol{L}_r^2};\ b=\frac{\boldsymbol{L}_m^2\boldsymbol{R}_r}{\sigma\boldsymbol{L}_r^2};\ c=\frac{1}{\sigma}. \tag{5}$$

The new expression of the electromagnetic torque and the slip frequency are given by:

$$T_e=\frac{3}{2}n_p\frac{M}{\boldsymbol{L}_r}\boldsymbol{\psi}_{rd}\boldsymbol{i}_{sq}, \tag{6}$$

$$\omega_{sl}=\frac{M}{\boldsymbol{L}_r}\boldsymbol{\psi}_{rd}\boldsymbol{i}_{sq}. \tag{7}$$

3 BS_NAHOSM control structure for FOC control of SPIM drives

3.1 BS design for the outer speed and flux loops

The enhanced BS controller adopted in this study is based on the structure proposed in Pham [20], with modifications to improve its robustness against parameter variations and external load disturbances. To achieve this, an integral term of the tracking error is incorporated into the design of the rotor flux and speed controllers. Furthermore, the controller leverages an online update of the rotor resistance to enhance adaptability. The stability and convergence of the control subsystems are rigorously verified through Lyapunov stability theory [2]. At each design stage, virtual control inputs are systematically introduced to guide the subsystem states toward their desired references, ensuring reliable and consistent performance.

The rotor flux and speed tracking errors is defined:

$$\begin{aligned}\varepsilon_\omega&=\left(\omega_r^*-\omega_r\right)+k'_\omega\int_0^t\left(\omega_r^*-\omega_r\right)dt\\ \varepsilon_\psi&=\left(\boldsymbol{\psi}_{rd}^*-\boldsymbol{\psi}_{rd}\right)+k'_\psi\int_0^t\left(\boldsymbol{\psi}_{rd}^*-\boldsymbol{\psi}_{rd}\right)dt\end{aligned}. \tag{8}$$

The error dynamical equations:

$$\begin{aligned}\dot{\varepsilon}_{\omega} &= \dot{\omega}_r^* - \frac{3}{2}P\frac{\delta\sigma \boldsymbol{L}_s}{J}\boldsymbol{\psi}_{rd}\boldsymbol{i}_{sq} + \frac{T_l}{J} + B\omega_r + k'_{\omega}\left(\omega_r^* - \omega_r\right) \\ \dot{\varepsilon}_{\psi} &= \dot{\boldsymbol{\psi}}_{rd}^* + \frac{\boldsymbol{L}_m}{\tau_r}\boldsymbol{i}_{sd} + \frac{1}{\tau_r}\boldsymbol{\psi}_{rd} + k'_{\psi}\left(\boldsymbol{\psi}_{rd}^* - \boldsymbol{\psi}_{rd}\right)\end{aligned}. \quad (9)$$

Lyapunov function is chosen:

$$\boldsymbol{V}_{(\omega,\psi)} = \frac{1}{2}\left(\varepsilon_{\omega}^2 + \varepsilon_{\psi}^2\right). \quad (10)$$

Differentiating $\boldsymbol{V}$:

$$\frac{d\boldsymbol{V}_{(\omega,\psi)}}{dt} = \varepsilon_{\omega}\frac{d\varepsilon_{\omega}}{dt} + \varepsilon_{\psi}\frac{d\varepsilon_{\psi}}{dt}. \quad (11)$$

where: $k_t = 3/2\ n_p \times \delta\sigma L_s/J$, k_{ω}, k_{ψ} are positive design constants that determine the closed-loop dynamics.

$$\begin{aligned}\frac{d\boldsymbol{V}_{(\omega,\psi)}}{dt} &= \varepsilon_{\omega}\left[\begin{array}{l}\dfrac{d\omega_r^*}{dt} - k_t\boldsymbol{\psi}_{rd}\boldsymbol{i}_{sq}^* + \dfrac{T_l}{J} \\ +B\omega_r + k'_{\omega}\left(\omega_r^* - \omega_r\right)\end{array}\right] \\ &+\varepsilon_{\psi}\left[\frac{d\boldsymbol{\psi}_{rd}^*}{dt} + \frac{\boldsymbol{L}_m}{\tau_r}\boldsymbol{i}_{sd}^* + \frac{1}{\tau_r}\boldsymbol{\psi}_{rd} + k'_{\psi}\left(\boldsymbol{\psi}_{rd}^* - \boldsymbol{\psi}_{rd}\right)\right].\end{aligned} \quad (12)$$

To $V' < 0$, the stabilizing virtual controls are chosen as:

$$\begin{aligned}\boldsymbol{i}_{sq}^* &= \frac{1}{k_t\boldsymbol{\psi}_{rd}}\left[k_{\omega}\varepsilon_{\omega} + \frac{d\omega_r^*}{dt} + \frac{T_L}{J} + B\omega_r + k'_{\omega}\left(\omega_r^* - \omega_r\right)\right] \\ \boldsymbol{i}_{sd}^* &= \frac{\tau_r}{\boldsymbol{L}_m}\left[k_{\psi}\varepsilon_{\psi} + \frac{d\boldsymbol{\psi}_{rd}^*}{dt} + \frac{1}{\tau_r}\boldsymbol{\psi}_{rd} + k'_{\psi}\left(\boldsymbol{\psi}_{rd}^* - \boldsymbol{\psi}_{rd}\right)\right]\end{aligned}. \quad (13)$$

T_L in Eq. (13) is estimated in Section 3. 2.

I obtain:

$$\frac{d\boldsymbol{V}_{(\omega,\psi)}}{dt} = -k_{\omega}\varepsilon_{\omega}^2 - k_{\psi}\varepsilon_{\psi}^2 < 0. \quad (14)$$

$\boldsymbol{i}_{sd}$ and $\boldsymbol{i}_{sq}$ virtual control vectors in Eq. (13) are chosen to satisfy the control objectives and these virtual components also provide as the reference inputs for the next step of the NAHOSM design.

3.2 Electromagnetic torque observer

Section 3.2 proposes an electromagnetic torque observer to estimate the component required for the BS_NAHOSM control strategy. This observer utilizes a predictive model, a concept previously detailed in Wang et al. [19]. The adoption of this predictive approach aims to achieve fast and accurate torque estimation while significantly reducing oscillations in the estimated torque signal. To implement the predictive algorithm within this observer, forward Euler discretization is employed for the system model:

$$\frac{dx}{dt} \approx \frac{x(k+1) - x(k)}{T_s}, \quad (15)$$

where T_s is the sampling time of the system.

The dynamic equations of the stator flux and the stator current of an Induction Motor (IM) in the stationary reference frame [23] are written as:

$$\begin{bmatrix}\dot{\hat{\boldsymbol{\varphi}}}_s \\ \dot{\hat{\boldsymbol{i}}}_s\end{bmatrix} = \begin{bmatrix}0 & -\boldsymbol{R}_s \\ A_{21} & A_{22}\end{bmatrix}\begin{bmatrix}\hat{\boldsymbol{\varphi}}_s \\ \hat{\boldsymbol{i}}_s\end{bmatrix} + \begin{bmatrix}1 \\ \dfrac{1}{\sigma\boldsymbol{L}_s}\end{bmatrix}\boldsymbol{v}_s, \quad (16)$$

with:

$$A_{21} = \frac{1}{\sigma\boldsymbol{L}_s}\left(\frac{1}{\tau_r} - j\omega_r\right) \text{ and } A_{22} = j\omega_r - \frac{1}{\sigma\tau_s} - \frac{1}{\sigma\tau_r},$$

where:

- $\boldsymbol{v}_s = v_{s\alpha} + v_{s\beta}$ represents the stator voltage;
- $\boldsymbol{i}_s = i_{s\alpha} + ji_{s\beta}$ is the stator current;
- $\hat{\boldsymbol{\varphi}}_s = \hat{\varphi}_{s\alpha} + j\hat{\varphi}_{s\beta}$ denotes the stator flux.

Note that subscripts α and β depict the stationary reference frame components.

The predictions of the stator flux and the stator current are obtained by using the forward Euler discretization method as follows:

$$\hat{\boldsymbol{\psi}}_{\boldsymbol{s}_{k+1}} = \hat{\boldsymbol{\psi}}_{\boldsymbol{s}_k} + T_s\left(\boldsymbol{u}_{\boldsymbol{s}_k} - \boldsymbol{R}_s\boldsymbol{i}_{\boldsymbol{s}_k}\right), \quad (17)$$

$$\hat{\boldsymbol{i}}_{\boldsymbol{s}_{k+1}} = T_s A_{21}\hat{\boldsymbol{\psi}}_{\boldsymbol{s}_k} + \left(1 + T_s A_{22}\boldsymbol{i}_{\boldsymbol{s}_k}\right) + \frac{T_s}{\sigma\boldsymbol{L}_s}\hat{\boldsymbol{u}}_{\boldsymbol{s}_k}. \quad (18)$$

By using the forward Euler discretization method, the electromagnetic torque is obtained as:

$$\hat{T}_{e_{k+1}} = \frac{3}{2}p\ \mathrm{IM}\left\{\hat{\boldsymbol{\psi}}_{\boldsymbol{s}_{k+1}} \times \hat{\boldsymbol{i}}_{\boldsymbol{s}_{k+1}}\right\}, \quad (19)$$

where p is the number of pole pairs.

3.3 Designing NAHOSM controller for the inner current loop control

NAHOSM controller for the inner current loop control in FOC vector control of SPIM drive. Stator current error is defined:

$$\begin{cases} \varepsilon_{i_{sd}} = \boldsymbol{i}_{\boldsymbol{sd}}^{*} - \boldsymbol{i}_{\boldsymbol{sd}} \\ \varepsilon_{i_{sq}} = \boldsymbol{i}_{\boldsymbol{sq}}^{*} - \boldsymbol{i}_{\boldsymbol{sq}} \end{cases}. \tag{20}$$

The nonlinear slip surface according to the current components is chosen as follows:

$$\begin{bmatrix} s_1 \\ s_2 \end{bmatrix} = \begin{bmatrix} \varepsilon_{i_{sd}} + \lambda_1 \cdot \int_0^t \left|\varepsilon_{i_{sd}}\right|^{1/2} sat\left(\varepsilon_{i_{sd}}\right) \\ \varepsilon_{i_{sq}} + \lambda_2 \cdot \int_0^t \left|\varepsilon_{i_{sq}}\right|^{1/2} sat\left(\varepsilon_{i_{sq}}\right) \end{bmatrix}, \tag{21}$$

where: $\lambda_1 > 0, \lambda_2 > 0$.

We select the Lyapunov function:

$$V = \frac{1}{2}\left(s_1^2 + s_2^2\right). \tag{22}$$

Differentiate both sides of Eq. (16) we get:

$$\frac{dV}{dt} = s_1 \frac{ds_1}{dt} + s_2 \frac{ds_2}{dt}. \tag{23}$$

To differentiate $V < 0$, The current error differential function is chosen as follows:

$$\begin{cases} \dfrac{ds_1}{dt} = -v_{i_{sd}}(t) \\ \dfrac{ds_2}{dt} = -v_{i_{sq}}(t) \end{cases}, \tag{24}$$

where: $v_{i_{sd}}(t)$ and $v_{i_{sq}}(t)$ are NAHOSM control functions and defined:

$$\begin{aligned} v_{i_{sd}}(t) &= \alpha_{sd} F_{sd}(t) \\ v_{i_{sq}}(t) &= \alpha_{sq} F_{sq}(t) \end{aligned},$$

where:

$$\begin{cases} \alpha_{sd} = \dfrac{1}{2} sat\left(\left|s_1\right|\right) + \dfrac{3}{2} k_1 \left|s_1\right|^{1/2} sat\left(\left|s_1\right|\right) + k_1^2 \left|s_1\right| \\ F_{sd}(t) = \dfrac{s_1'' + 2\left(s_1' + \left|s_1\right|^{2/3} sat\left(s_1\right)\right)\left(\left|s_1'\right| + \left|s_1\right|^{2/3}\right)^{-1/2}}{\left|s_1''\right| + 2\left(\left|s_1'\right| + \left|s_1\right|^{2/3}\right)^{1/2}} \\ \alpha_{sq} = \dfrac{1}{2} sat\left(\left|s_2\right|\right) + \dfrac{3}{2} k_2 \left|s_2\right|^{1/2} sat\left(\left|s_2\right|\right) + k_2^2 \left|s_2\right| \\ F_{sq}(t) = \dfrac{s_2'' + 2\left(s_2' + \left|s_2\right|^{2/3} sat\left(s_2\right)\right)\left(\left|s_2'\right| + \left|s_2\right|^{2/3}\right)^{-1/2}}{\left|s_2''\right| + 2\left(\left|s_2'\right| + \left|s_2\right|^{2/3}\right)^{1/2}} \end{cases}, \tag{25}$$

with: $k_1 > 0; k_2 > 0$.

From Eqs. (4), (23), (24) and (25) we get $\boldsymbol{u}_{\boldsymbol{sd}}$ and $\boldsymbol{u}_{\boldsymbol{sq}}$ virtual control functions:

$$\begin{cases} \boldsymbol{u}_{\boldsymbol{sd}} = \dfrac{\boldsymbol{L}_s}{c}\left[\dfrac{d\boldsymbol{i}_{\boldsymbol{sd}}^{*}}{dt} + v_{i_{sd}}(t)\right] \\ \quad + \dfrac{1}{c}\left[a\boldsymbol{i}_{\boldsymbol{sd}} - \boldsymbol{L}_s \omega_e \boldsymbol{i}_{\boldsymbol{sq}} - b\boldsymbol{R}_r \boldsymbol{\psi}_{\boldsymbol{rd}}\right] \\ \boldsymbol{u}_{\boldsymbol{sq}} = \dfrac{\boldsymbol{L}_s}{c}\left[\dfrac{d\boldsymbol{i}_{\boldsymbol{sq}}^{*}}{dt} + v_{i_{sq}}(t)\right] \\ \quad + \dfrac{1}{c}\left[a\boldsymbol{i}_{\boldsymbol{sq}} - \boldsymbol{L}_s \omega_e \boldsymbol{i}_{\boldsymbol{sd}} - b\omega_e \boldsymbol{\psi}_{\boldsymbol{rd}}\right] \end{cases}. \tag{26}$$

4 Simulink and discussion

The performance of the proposed BS_NAHOSM hybrid controller for FOC of SPIM drives is validated through MATLAB/Simulink [25] simulations. Three case Tests were carried out including dynamic speed reversal under load disturbance, robustness to load disturbance, and robustness against electrical parameter variation at low and high speeds. All tests are compared with the BS_SOSM, BS_INTSM, PI controllers and compared with other latest methods [3, 5, 17, 20, 21] to confirm quantify the effectiveness of the proposed control structure. The block diagram of the SPIM drive system is shown in Fig. 3. The SPIM used in the simulation is a 1 HP, 6-phase machine with the following specifications: 220 V, 50 Hz, 4 pole, 1480 rpm, $\boldsymbol{R}_s$ = 10.1 W, $\boldsymbol{R}_r$ = 9.8546 W, $\boldsymbol{L}_s$ = 0.833457 H, $\boldsymbol{L}_r$ = 0.830811 H, $\boldsymbol{L}_m$ = 0.783106 H, J = 0.0088 kg m^2. $\boldsymbol{R}_s$, $\boldsymbol{R}_r$ is nominal value of rotor and stator resistance.

4.1 Case 1

To verify the dynamic performance of BS_NAHOSM, a survey of the start up and reversing modes is performed. The reference speed changes from 0 to +150 rad/s at

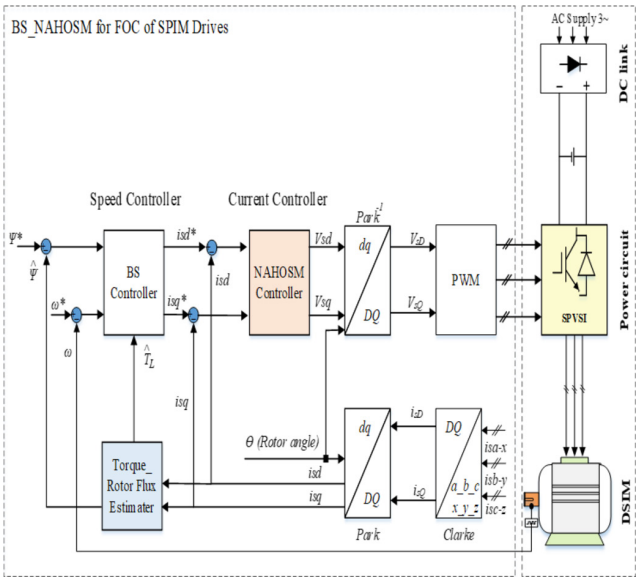

Fig. 3 Diagram of BS_NAHOSM vector control for SPIM drives

t = 0.25 s then reversing to −150 rad/s at t = 1 s and reducing to 0 at t = 2 s. A rated step load torque is applied at t = 0.7 s and rejected at t = 1.7 s to assess disturbance rejection under dynamic conditions. This survey is also carried out with the PI, BS_INTSM, BS_SOSM [20] controller to get comparison data.

Observing the obtained results shows that all three controllers achieved satisfactory reference tracking during the speed reversal. However, the proposed BS_NAHOSM controller exhibited significantly superior performance. The startup times and the reversal times for BS_NAHOSM, BS_SOSM, BS_INTSM and PI were 0.078 s, 0.103 s, 0.1033 s and 0.125 s and were 0.099 s, 0.129 s, 0.147 s, 0.85 s respectively, 0.12 s, 0.18 s, and 0.25 s. These results in Table 1 confirm the faster dynamic response of BS_NAHOSM. Moreover, the torque waveform of BS_NAHOSM exhibited no chattering and negligible ripple, in contrast to BS_SOSM and BS_INTSM, which showed noticeable torque oscillations during reversal Fig. 4 (c) and (d).

These results highlight the superior ability of BS_NAHOSM to provide faster and more accurate transient response, smoother dynamic behavior, enhanced stability, and strong disturbance rejection. Collectively, these advantages clearly demonstrate improved robustness and control precision of the proposed strategy compared to PI, conventional SOSM, and INTSM approaches.

When compared with the fuzzy-based FSOSMC controller presented in Finch and Giaouris [2], the ST-SMC Twelve-Sector DTC method in Zahraoui et al. [17], and the HOSTA controller in Karboua et al. [5], it is evident that these controllers also demonstrate good speed reversal performance. However, the significant torque ripple, flux oscillations, and chattering phenomena have been recorded.

In contrast, the proposed BS_NAHOSM controller delivers faster transient response, tighter reference tracking, and remarkably smoother torque behavior, minimal ripple and effectively eliminates chattering, confirming the advanced performance of HOSM-based strategies.

4.2 Case 2

In this case, the SPIM drive operates at high constant speed (155 rad/s) and the load torque changes (rated load torque is applied and rejected at t = 0.7 s and 1.7 s). Fig. 5 shows that BS_NSTA-SOSM is robust, stable against load disturbance variations. Compared to BS_SOSM [20], BS_INTSM and PI the phenomenon of torque and speed oscillations are significantly reduced, and the chattering phenomenon of BS_NSTA-SOSM is almost eliminated. The response speed is faster and more sustainable, SS error is almost zero Fig. 5 (a).

Compared with the HOSTA controller in Karboua et al. [5] and FSTASMC controller proposed in Farid et al. [21], it is evident that although HOSTA and FSOSMC controllers can manage load disturbances, the BS_NSTA-SOSM controller exhibits superior performance. It achieves faster convergence to the reference speed, lower speed drop when subjected to sudden load disturbances. In contrast, the FSOSMC controller experiences a noticeable speed drop and fails to accurately recover to the reference speed, as shown in Farid et al. [21] and in Karboua et al. [5]. Moreover, Farid et al. [21] reports significant torque and flux oscillations, while Karboua et al. [5] does not provide electromagnetic torque analysis. In contrast, the BS_NSTA-SOSM controller maintains stable speed, torque, and rotor flux responses without oscillations. Additionally, it effectively eliminates the chattering phenomenon, demonstrating its robustness and control precision under challenging operating conditions.

4.3 Case 3

To more clearly prove the robustness of the BS_NSTA-SOSM controller against load disturbances and the impact of machine parameter changes, another survey was also performed under load disturbance conditions, machine parameters $\boldsymbol{R}_s$, $\boldsymbol{R}_r$ have been changed in the high and low speed range. Two test cases have been carried up under the same conditions at low speed (25 rad/s) and high speed (100 rad/s). Initially, the stator $\boldsymbol{R}_s$ and rotor $\boldsymbol{R}_r$ resistances are at

Table 1 Control quality parameters in test 1

	BS_NAHOSM	BS_SOSM	BS_INTSM	PI
Start-up times (s)	0.071	0.103	0.1033	0.125
Stable times (s)	0.003	0.0005	0.0055	0.035
Reversal times (s)	0.099	0.129	0.147	0.85
Drop speed (rad/s))	1.09	−1.5	−1.55	−4.8
Recovery time (s)	0.008	0.02	0.026	0.059

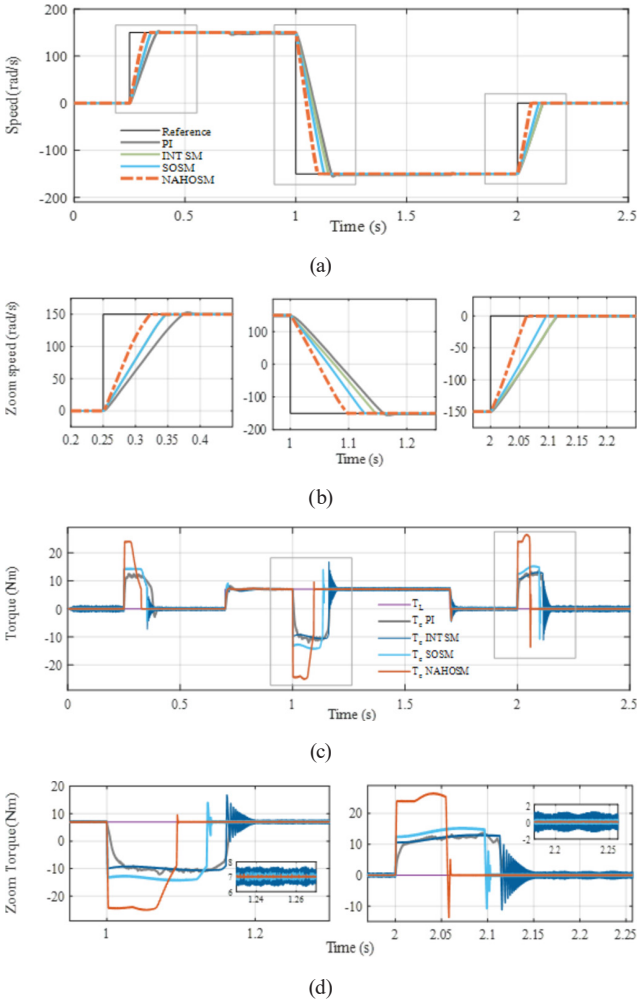

Fig. 4 Case in SPIM drives work in reversal conditions, load disturbance of PI, BS_INTSM, BS_SOSM and BS_NAHOSM controllers: (a) Speed responses; (b) Zoomed-in speed responses; (c) Torque responses; (d) Zoomed-in torque responses

their nominal value. At t = 1.0 s, they increase by 25% $\left(\boldsymbol{R}_r = 1.25\ \boldsymbol{R}_r^*,\ \boldsymbol{R}_s = 1.25\ \boldsymbol{R}_s^*\right)$, at t = 1.5 s, they are increase of 100% $\left(\boldsymbol{R}_r = 2\ \boldsymbol{R}_r^*,\ \boldsymbol{R}_s = 2\ \boldsymbol{R}_s^*\right)$. Finally, at t = 2 s, both resistances return to their nominal value $\left(\boldsymbol{R}_r = \boldsymbol{R}_r^*,\ \boldsymbol{R}_s = \boldsymbol{R}_s^*\right)$, as illustrated in Fig. 6 (f). In addition to parameter variation, a step load disturbance from 0 to 100% of the rated torque was applied at t = 0.2 s and maintained for the remainder of the simulation process. The effects of these disturbances on system performance are shown in Fig. 6 (c) for low speed and Fig. 7 (c) for high speed. These same test conditions across two speed ranges provide a consistent basis for evaluating the controller's resilience under combined electrical and mechanical disturbance.

As shown in Figs. 6 and 7, the PI controller is highly sensitive to both parameter variations and external load disturbances. It fails to maintain the reference speed is 25 rad/s at low speed (Fig. 6 (a)) and 100 rad/s at high

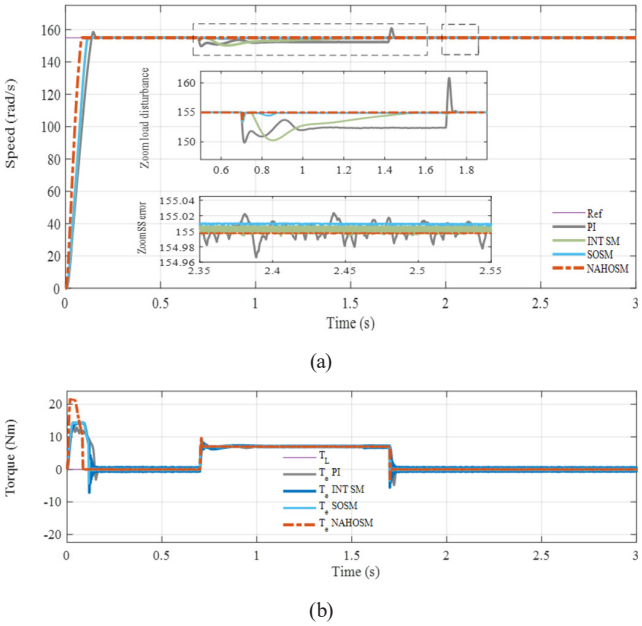

Fig. 5 Response of speed under load torque disturbance of the PI, BS_INTSM, BS_SOSM and BS_NAHOSM controllers: (a) Speed responses and zoomed-in speed responses; (b) Torque responses

speed (Fig. 7(a)) – when a step load torque is applied at t = 0.25 s. In particular, when motor parameters are varied, significant speed oscillations and high torque ripple are observed in Fig. 6 (a) to (c) and Fig. 7(a) and to (c). The BS_INTSM controller performs better than PI, maintaining the speed closer to the reference under parameter changes and load application at t = 0.25 s, especially when $\boldsymbol{R}_s$ and $\boldsymbol{R}_r$ increase by 25% and 100% at low speed, and by 25% at high speed.

However, at t = 1.5 s, when $\boldsymbol{R}_s$ and $\boldsymbol{R}_r$ increase to 200% of nominal at high speed, the BS_INTSM controller experiences a speed drop of 0.171 rad/s (1.71%) with a recovery time of 0.55 s. The rotor flux also drops by 0.18 Wb (0.18%), recovering in 0.02 s when motor parameter returns to normal values at t = 2 s. Moreover, zoomed views of the speed and torque responses reveal pronounced ripples under both low-speed (Fig. 6 (b) and (c)) and high-speed (Fig. 7 (b) and (c)) conditions. These fluctuations can negatively impact the mechanical system and degrade drive efficiency.

In contrast, the proposed BS_NAHOSM controller demonstrates the best overall performance. It offers superior robustness and precision, with minimal speed deviation, and exhibits smooth and stable torque and flux responses. The high-order sliding mode design helps effectively eliminates chattering.

A comparison of the results in Fig. 6 (a) to (c) with those in Kiyyour et al. [3] confirms that, even under more severe test conditions, the BS_NSTA-SOSM controller achieves better

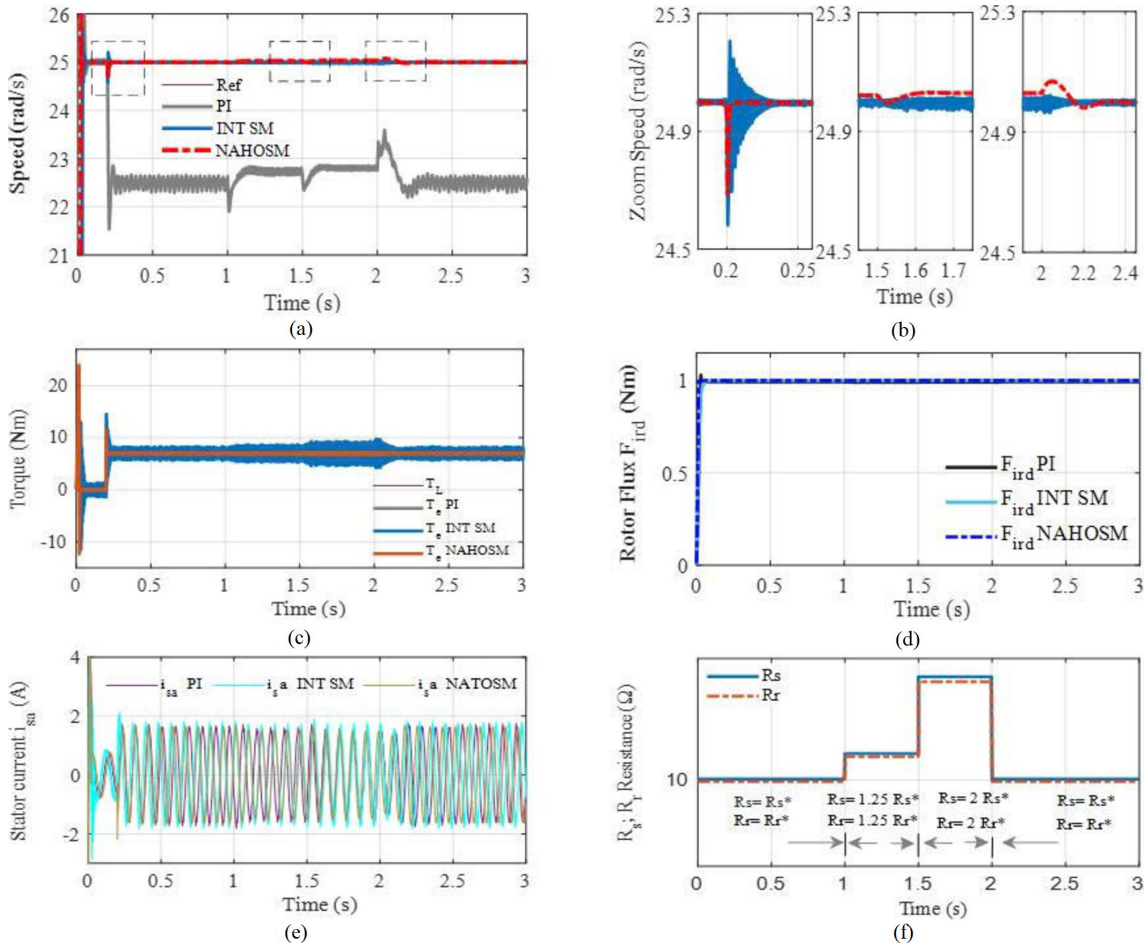

Fig. 6 Response of speed, torque, flux when parameters $\boldsymbol{R_s}$, $\boldsymbol{R_r}$ change (low speed): (a) Speed responses; (b) Zoomed-in speed responses; (c) Torque responses; (d) Rotor flux magnitude responses; (e) Stator current responses; (f) Variation of stator and rotor resistances

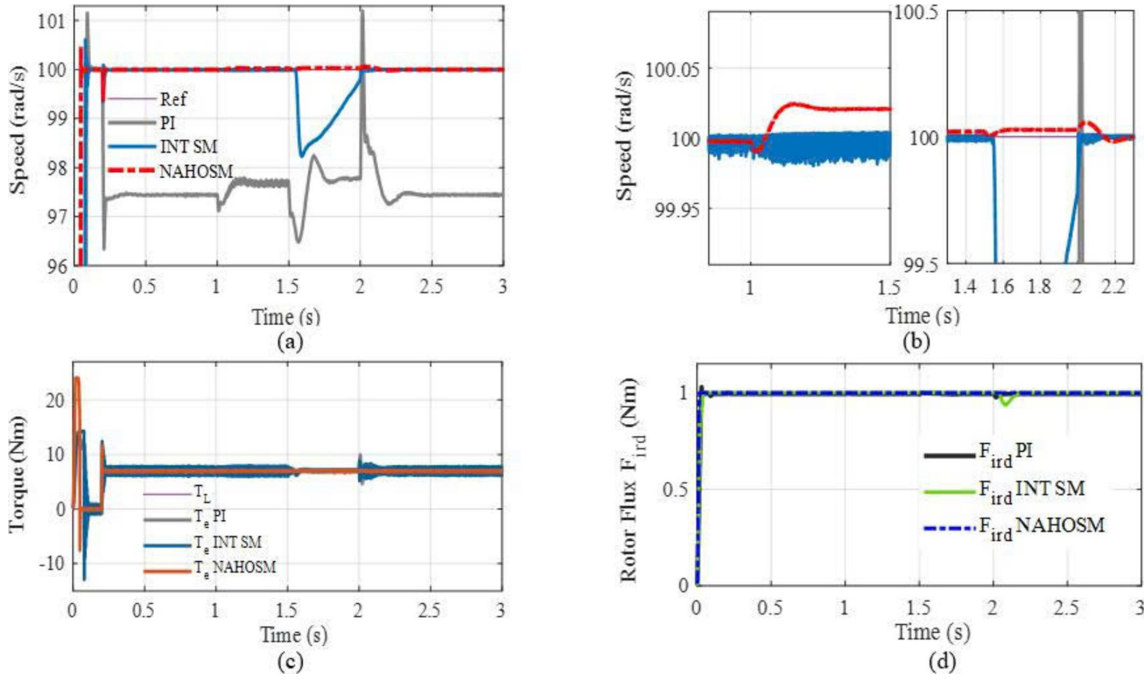

Fig. 7 Response of speed, torque, flux when parameters $\boldsymbol{R_s}$, $\boldsymbol{R_r}$ change (high speed): (a) Speed responses; (b) Zoomed-in speed responses; (c) Torque responses; (d) Rotor flux magnitude responses

speed and torque responses than the PSO-based controller. In Kiyyour et al. [3], the torque oscillations was recorded.

5 Conclusion

This paper proposed an improved BS_NSTA-SOSM hybrid control structure for FOC of SPIM drives. The controller effectively integrates BS control for the outer loops and a NAHOSM for the inner current loop. The simulation tests were conducted under various operating conditions to assess the robustness and dynamic performance of the proposed method. The results demonstrate that the BS_NSTA-SOSM controller significantly outperforms conventional PI, BS_INTSM, and other recently published control strategies [3, 5, 17, 20, 21]. It provides faster transient response, superior steady-state accuracy, and enhanced robustness against external disturbances and parameter variations. Notably, the proposed controller effectively suppresses the chattering phenomenon, which is a common issue in sliding mode-based strategies. The BS_NSTA-SOSM proposed control structure offers a promising solution for high-performance SPIM drive systems, ensuring enhanced control quality, system stability, and operational reliability under real-world conditions.

References

[1] Ayala, M., Doval-Gandoy, J., Rodas, J., Gonzalez, O., Gregor, R., Delorme, L., Romero, C., Fleitas, A. "Field-Weakening Strategy with Modulated Predictive Current Control Applied to Six-Phase Induction Machines", Machines, 12(3), 178, 2024. https://doi.org/10.3390/machines12030178

[2] Finch, J. W., Giaouris, D. "Controlled AC Electrical Drives", IEEE Transactions on Industrial Electronics, 55(2), pp. 481–491, 2008. https://doi.org/10.1109/TIE.2007.911209

[3] Kiyyour, B., Laggoun, L., Salhi, A., Naimi, D., Boukhalfa, G. "Improvement DTC for Induction Motor Drives Using Modern Speed Controllers Tuning by PSO Algorithm", Periodica Polytechnica Electrical Engineering and Computer Science, 67(3), pp. 249–259, 2023. https://doi.org/10.3311/PPee.21000

[4] Pham, N. T., Le, T. D. "A Novel FOC Vector Control Structure Using RBF Tuning PI and SM for SPIM Drives", International Journal of Intelligent Engineering & Systems, 13(5), pp. 429–440, 2020. https://doi.org/10.22266/ijies2020.1031.38

[5] Karboua, D., Toual, B., Kouzou, A., Douara, B. O., Mebkhouta, T., Bendenidina, A. N. "High-order Supper-twisting Based Terminal Sliding Mode Control Applied on Three Phases Permanent Synchronous Machine", Periodica Polytechnica Electrical Engineering and Computer Science, 67(1), pp. 40–50, 2023. https://doi.org/10.3311/PPee.21026

[6] Pham, N. T., Le, T. D. "A Novel Improved VGSTA BS_SM Control Structure for Vector Control of High Performance SPIM Drives", International Journal of Intelligent Engineering and Systems, 15(1), pp. 155–166, 2022. https://doi.org/10.22266/ijies2022.0228.15

[7] Wang, T., Wang, B., Yu, Y., Xu, D. "A Closed-Loop Voltage Model Observer for Sensorless Induction Motor Drives Based on the Orthogonality and Sliding-Mode Technique", IEEE Transactions on Industrial Electronics, 71(11), pp. 13693–13707, 2024. https://doi.org/10.1109/TIE.2024.3374363

[8] Zhang, Y., Yan, Q., Ai, C., Wang, Y., Han, P., Zhou, Q., Du, G. "Backstepping control of permanent magnet synchronous motors based on load adaptive fuzzy parameter online tuning", Journal of Power Electronics, 24(7), pp. 1059–1070, 2024. https://doi.org/10.1007/s43236-024-00790-9

[9] Jang, S. G., Yoo, S. J. "Predefined-time synchronized backstepping control of strict feedback nonlinear systems", International Journal of Robust and Nonlinear Control, 33(13), pp. 7563–7582, 2023. https://doi.org/10.1002/rnc.6765

[10] Traoré, D., de Leon, J., Glumineau, A. "Sensorless induction motor adaptive observer-backstepping controller: experimental robustness tests on low frequencies benchmark", IET Control Theory & Applications, 4(10), pp. 1989–2002, 2010. https://doi.org/10.1049/iet-cta.2009.0648

[11] Rinkeviciene, R., Mitkiene, B. "Design and Analysis Models with PID and PID Fuzzy Controllers for Six-Phase Drive", World Electric Vehicle Journal, 15(4), 164, 2024. https://doi.org/10.3390/wevj15040164

[12] Liu, X., Deng, Y., Wang, J., Li, H., Cao, H. "Fixed-Time Generalized Active Disturbance Rejection With Quasi-Resonant Control for PMSM Speed Disturbances Suppression", IEEE Transactions on Power Electronics, 39(6), pp. 6903–6918, 2024. https://doi.org/10.1109/TPEL.2024.3377186

[13] Kali, Y., Rodas, J., Doval-Gandoy, J., Ayala, M., Gonzalez, O. "Enhanced Reaching-Law-Based Discrete-Time Terminal Sliding Mode Current Control of a Six-Phase Induction Motor", Machines, 11(1), 107, 2023. https://doi.org/10.3390/machines11010107

[14] Bhaumik, A., Das, S. "Virtual voltage vector based predictive current control of speed sensorless induction motor drives", ISA Transactions, 133, pp. 495–504, 2023. https://doi.org/10.1016/j.isatra.2022.07.007

[15] Zellouma, D., Bekakra, Y., Benbouhenni, H. "Performance Improvement of Rotor Flux and Electromagnetic Torque Control in Induction Motors using the Backstepping Super-Twisting Algorithm", Journal of Electrical Engineering, Electronics, Control and Computer Science (JEEECCS), 9(3), pp. 19–30, 2023. [online] Available at: https://jeeeccs.org/jeeeccs/index.php/journal/article/view/345 [Accessed: 11 May 2024]

[16] Zaafouri, A., Regaya, C. B., Azza, H. B., Châari, A. "DSP-based adaptive backstepping using the tracking errors for high performance sensorless speed control of induction motor drive", ISA Transactions, 60, pp. 333–347, 2016. https://doi.org/10.1016/j.isatra.2015.11.021

[17] Zahraoui, Y., Moutchou, M., Tayane, S., Fahassa, C., Elbadaoui, S. "Induction Motor Performance Improvement using Super Twisting SMC and Twelve Sector DTC", International Journal of Robotics and Control Systems, 4(1), pp. 50–68, 2024. https://doi.org/10.31763/ijrcs.v4i1.1090

[18] Li, H., Chou, W. "Adaptive FNN Backstepping Control for Nonlinear Bilateral Teleoperation With Asymmetric Time Delays and Uncertainties", International Journal of Control, Automation and Systems, 21(9), pp. 3091–3104, 2023. https://doi.org/10.1007/s12555-022-0158-9

[19] Wang, F., Li, S., Mei, X., Xie, W., Rodríguez, J., Kennel, R. M. "Model-Based Predictive Direct Control Strategies for Electrical Drives: An Experimental Evaluation of PTC and PCC Methods", IEEE Transactions on Industrial Informatics, 11(3), pp. 671–681, 2015. https://doi.org/10.1109/TII.2015.2423154

[20] Pham, N. T. "Speed Tracking of Field Oriented Control SPIM Drive using (BS_SOSM) Nonlinear Control Structure", WSEAS Transactions on Systems and Control, 14, pp. 291–299, 2019. [online] Available at: https://www.wseas.org/multimedia/journals/control/2019/a745103-871.pdf [Accessed: 11 May 2024]

[21] Farid, B., Tarek, B., Sebti, B. "Fuzzy super twisting algorithm dual direct torque control of doubly fed induction machine", International Journal of Electrical and Computer Engineering (IJECE), 11(5), pp. 3782–3790, 2021. https://doi.org/10.11591/ijece.v11i5.pp3782-3790

[22] Zellouma, D., Benbouhenni, H., Bekakra, Y. "Backstepping Control Based on a Third-order Sliding Mode Controller to Regulate the Torque and Flux of Asynchronous Motor Drive", Periodica Polytechnica Electrical Engineering and Computer Science, 67(1), pp. 10–20, 2023. https://doi.org/10.3311/PPee.20333

[23] Pham, N. T. "Sensorless speed control of SPIM using BS_PCH novel control structure and NNSM_SC MRAS speed observer", Journal of Intelligent & Fuzzy Systems, 39(3), pp. 2657–2677, 2020. https://doi.org/10.3233/JIFS-190540

[24] Derbel, N., Ghommam, J., Zhu, Q. "Applications of Sliding Mode Control", Springer Singapore, 2017. ISBN 978-981-10-2373-6 https://doi.org/10.1007/978-981-10-2374-3

[25] The MathWorks, Inc. "MATLAB and Simulink, (R2023b)", [computer program] Available at: https://www.mathworks.com/products/new_products/release2023b.html [Accessed: 11 May 2024]